System Advantages of Using Large-Scale Aperiodic Array Topologies in Future mm-Wave 5G/6G Base Stations

An Interdisciplinary Look

Aslan, Yanki; Roederer, Antoine; Yarovoy, Alexander

DOI
10.1109/JSYST.2020.3045909

Publication date
2022

Document Version
Final published version

Published in
IEEE Systems Journal

System Advantages of Using Large-Scale Aperiodic Array Topologies in Future mm-Wave 5G/6G Base Stations: An Interdisciplinary Look

Yanki Aslan, *Graduate Student Member, IEEE*, Antoine Roederer, *Life Fellow, IEEE*, and Alexander Yarovoy, *Fellow, IEEE*

***Abstract*—The encouraging potential of employing large-scale aperiodic base station arrays in addressing the radiation pattern and thermal requirements of the next generation communication systems is demonstrated. Sample 256-element layout-optimized multibeam arrays are presented as a futuristic view. The system benefits (in terms of the statistical quality-of-service, energy efficiency, thermal management, and processing burden) of the proposed arrays, as well as their performance versus design complexity tradeoffs, are explained through interdisciplinary simulations. The key advantage of the proposed antennas over the currently proposed 64-element periodic arrays is identified as the increased gain with much lower side lobes, which yields much less power and less heat per element with more surface for cooling, and allows robust/computationally efficient precoding.**

***Index Terms*—5G/6G communications, antenna synthesis, aperiodic array, array cooling, layout optimization, system analysis.**

I. Introduction

THE demanding system performance requirements of the next-generation mm-wave communication networks make the antenna synthesis and beamforming an interdisciplinary optimization problem [1]. In addition to the electromagnetic aspects (i.e., related to the array radiation pattern characteristics), such an optimization procedure must consider complementary research domains including, but not limited to the following.

1) *Signal Processing*, due to the large amount of control parameters in arrays with limited processing power and speed.
2) *Front-End Circuitry and Hardware*, due to the compact system integration challenges, component (and cost) reduction requirements.
3) *Thermal Management*, due to the low efficiency of power amplifiers (PAs), high spatial density of the heat sources, and higher heat generation than the conventional systems [2], [3].
4) *Medium Access Control*, due to the need to manage multiple data streams to simultaneous users, where each user receives a dedicated cofrequency beam [4].

For each domain listed above, there is a direct relation between the desired performance level and the total number of active elements in the antenna array. The baseline in the state-of-the-art mm-wave 5G base station antenna arrays from leading companies, such as Ericsson [5], Nokia [6], IBM [7], NXP [8], and NEC [9], is to use a maximum of 64 elements, in a dense (around 0.5λ-spaced) and periodic arrangement. Then, the question arises: Is this the optimal element number and array configuration from the system perspective?

Indeed, fully populated equally spaced array in a rectangular or hexagonal topology can be considered as the current reference for base station antennas. However, as compared to such standard topologies, aperiodic/sparse layout-optimized arrays can (simultaneously) [10]

1) improve total signal-to-interference-plus-noise ratio (SINR) by preserving the gain while lowering the side lobes within the same scanning area, the extent of which depends on the number of elements and the available aperture size;
2) decrease the maximal temperature of the beamforming chips, the extent of which depends on the sparsity of the array and the thermal properties of the integrated circuits (ICs)/boards;
3) provide more space for placing the electronics and for circuit routing.

Such "unconventional" array topologies have gained more attention in the last few years as a potential breakthrough for the next-generation communication systems, with already demonstrated concepts recently presented in the literature [11], [12].

In our previous study [13], by taking a topology-optimized 64-element integrated array as the reference, we have investigated the effect of element number reduction on the interbeam interference and IC temperatures. From the simulation results, the following is clearly evident:

i) for such small or moderate size arrays (i.e., with ≤ 64 elements), the use of an external heatsink (which can be very large and bulky [14]) is a must for passive-only cooling;

Manuscript received August 3, 2020; revised November 17, 2020; accepted December 16, 2020. Date of publication January 11, 2021; date of current version March 24, 2022. This work was supported in part by the Netherlands Organisation for Scientific Research, and in part by NXP Semiconductors in the framework of the partnership program on Advanced 5G Solutions within the project number 15590 entitled "Antenna Topologies, and Front-end Configurations for Multiple Beam Generation". *(Corresponding author: Yanki Aslan.)*

The authors are with the Department of Microelectronics, Microwave Sensing, Signals and Systems Group, Delft University of Technology, Delft, GA 2600, The Netherlands (e-mail: Y.Aslan@tudelft.nl; A.G.Roederer@tudelft.nl; A.Yarovoy@tudelft.nl).

Digital Object Identifier 10.1109/JSYST.2020.3045909

ii) the number of elements can be reduced up to a certain extent (for design/beamforming simplification), with low impact on the electromagnetic and thermal performance. Further thinning causes an increase in the side lobe levels (SLLs) and IC temperatures.

Besides, for smaller-sized arrays for 5G antenna systems, more powerful PAs need to be used to satisfy the effective isotropic radiated power (EIRP) requirements. This poses challenges in terms of the availability in the low-cost CMOS technology and on the thermal control due to the generation of more heat per element [15].

An opposite approach would be to increase the number of elements to achieve more gain, lower side lobes; thus much less power and less heat per chip with more surface for cooling. For example, when compared to the 64-element aperiodic array, an optimized 256-element array (with a similar average interelement spacing) has [16]–[18] the following:

1) four times the gain and better angular resolution;
2) 1/4 of the radiated power (thus with 1/16 of the power per PA) to serve the same number of users;
3) 6 dB (or more) additional SLL suppression (similar to or better than the random arrays). Thus, the absolute level of the side lobes remains similar to the one of the 64-element aperiodic array, but the power flow toward the side lobes decreases by about 6 dB due to four times less total PA output power;
4) four times the area to dissipate 1/4 of the heat.

It is also very important to note that the large-scale arrays have a key advantage on reducing the electricity consumption, with the help of the high antenna gain and low side lobes.

Few companies (such as Anokiwave [19]) have already released 256-element active antenna arrays for mm-wave 5G. However, the array designs are based on regular square-grid dense topologies with high side lobes, whereas, as already mentioned, the aperiodic/sparse arrays have key advantages on interference suppression and additional thermal handling.

In this article, we present novel large-scale (256-element) irregular array layouts that are optimized for the (statistically) highest in-sector interference suppression and that can potentially achieve fullypassive cooling without an external heatsink. Moreover, the system advantages and performance tradeoffs of the proposed arrays are discussed in detail from an interdisciplinary (electromagnetic, thermal, and communication system) perspective.

Although the proposed concept has a big potential for addressing the thermal issue, due to the increased hardware and design complexity with more elements, synthesis of large scale aperiodic arrays can be considered as a futuristic view, which would be suitable for the next phase of the 5G radios.

The rest of this article is organized as follows. Section II presents the approaches and settings used in the electromagnetic, communication system, and thermal simulations. The simulation results are shown and discussed in Section III. Finally, Section IV concludes this article.

The general symbols and operators used in this article are explained in Table I.

TABLE I
EXPLANATION OF THE SYMBOLS AND OPERATORS USED IN THIS ARTICLE

Symbol or Operator	Definition
a, A	scalar
a^n, A^n	value to the power n
$\|a\|$, $\|A\|$	absolute value
$\hat{a}$	unit vector (direction)
$\boldsymbol{A}$	matrix
$C^{\,m\times n}$	complex-valued matrix with m rows and n columns
$\boldsymbol{A}^{-1}$	inverse of a matrix
$\boldsymbol{A}^{\dagger}$	conjugate transpose of a matrix
$\boldsymbol{a}$	vector
$a(.)$, $A(.)$	function
$a^{(n)}$, $A^{(m,n)}$, $a^{(m,n)}(.)$	single (n-th) or multi-dimensional (m,n-th) state of a vector, matrix or function
a_n, $A_{m,n}$, $a_n(.)$	n-th element of the vector $\boldsymbol{a}$, element in the m-th row and n-th column in matrix $\boldsymbol{A}$, the n-th distribution of a function $a(.)$
$>,<,\geq,\leq$	component-wise inequality
$\in$	belong to

II. SIMULATION APPROACH AND SETTINGS

A. Electromagnetic Aspects

For the optimization of the array layouts, the uniform-amplitude aperiodic array synthesis technique based on iterative convex element position perturbations [10] is used in this article. Therefore, in this section, a brief summary of the synthesis procedure is given and the settings used for the optimization are listed.

Let us consider a pregiven 2-D initial array layout (on the xy-plane) with a total number of N antenna elements (i.e., $n = 1, 2, \ldots, N$). Let us further assume that at the ith step of the algorithm, the nth element is moved by $\epsilon_n^{(i)}$ in the $\hat{\text{x}}$direction (i.e., $x_n^{(i)} = x_n^{(i-1)} + \epsilon_n^{(i)}$) and $\delta_n^{(i)}$ in the $\hat{\text{y}}$ direction (i.e., $y_n^{(i)} = y_n^{(i-1)} + \delta_n^{(i)}$). For sufficiently small perturbations on the element locations (i.e., when $|(\epsilon, \delta)_n^{(i)}| \ll \lambda/2\pi = 0.16\lambda$ [20], where λ is the wavelength at the operating frequency), the far field function can be linearized around the element positions using the first-order Taylor expansion. Assuming uniform amplitudes, linear phase shifts for beam scanning, and ignoring the sufficiently small higher order terms $(\epsilon_n^{(i)})^2$, $(\delta_n^{(i)})^2$, $(\epsilon_n^{(i)}\delta_n^{(i)})$, the following approximate relation is obtained [10]:

$$f_{\epsilon_n,\delta_n}^{(i,s)}(u,v) \approx \frac{1}{N}\sum_{n=1}^{N} E_n^{(i)}(u,v) e^{jk((u-u_s)x_n^{(i-1)}+(v-v_s)y_n^{(i-1)})} \left(1 + jk(u-u_s)\epsilon_n^{(i)} + jk(v-v_s)\delta_n^{(i)}\right) \quad (1)$$

where $f_{\epsilon_n,\delta_n}^{(i,s)}(u,v)$ is the normalized far field of the array at the ith iteration of the algorithm for a scanned beam, s ($s = 1, 2, \ldots, S$) in $u = \sin\theta\cos\phi, v = \sin\theta\sin\phi$ plane coordinates. k represents the wavenumber, which is equal to $2\pi/\lambda$. $E_n^{(i)}(u,v)$ denotes the embedded element pattern of the nth element at the ith iteration.

It is further required to define the side lobe region of each scanned beam, $s = 1, \ldots, S$. Although it changes with scanning, the side lobe regions (by assuming a circular beam shape) can be roughly taken as in (2) according to a main lobe radius, r, which is about λ/D radians (i.e., the first null position and about

4 dB beamwidth), where D is the array's side length

$$(u,v) \in (\boldsymbol{u},\boldsymbol{v})_{SL,s} \; if \; (u-u_s)^2+(v-v_s)^2 > r^2. \quad (2)$$

Finally, a constraint on the minimal element separation, $d_{\min}$ is defined for every element pair (α,β) as shown in (3), which is an approximation to the standard Euclidian distance inequality [10]

$$(\epsilon_\alpha^{(i)}-\epsilon_\beta^{(i)})(2x_\alpha^{(i-1)}-2x_\beta^{(i-1)})+(\delta_\alpha^{(i)}-\delta_\beta^{(i)})(2y_\alpha^{(i-1)}-2y_\beta^{(i-1)}) + (x_\alpha^{(i-1)}-x_\beta^{(i-1)})^2+(y_\alpha^{(i-1)}-y_\beta^{(i-1)})^2 \geq d_{\min}^2. \quad (3)$$

Overall, the compact optimization problem is formulated as

$$\min_{\boldsymbol{\epsilon}^{(i)},\boldsymbol{\delta}^{(i)}} \rho, \text{ s.t. } \begin{cases} |f_{\boldsymbol{\epsilon}^{(i)},\boldsymbol{\delta}^{(i)}}^{(i,u_s,v_s)}((\boldsymbol{u},\boldsymbol{v})_{SL,s})| \leq \rho \text{ holds } \forall s \\ |\boldsymbol{\epsilon}^{(i)}| \leq \mu, \; |\boldsymbol{\delta}^{(i)}| \leq \mu \\ (3) \text{ holds } \forall(\alpha,\beta) \in \{1,\ldots,N\}, \alpha \neq \beta \end{cases} \quad (4)$$

where $\boldsymbol{\epsilon}^{(i)} = \begin{bmatrix} \epsilon_1^{(i)} & \cdots & \epsilon_N^{(i)} \end{bmatrix}$ and $\boldsymbol{\delta}^{(i)} = \begin{bmatrix} \delta_1^{(i)} & \cdots & \delta_N^{(i)} \end{bmatrix}$. ρ denotes the maximal SLL, which is simultaneously minimized for all the scan angles specified at the algorithm input. μ is the user-defined upper bound for the position shifts to validate the approximation in (1) and to achieve fast and stable convergence. Note that it is also possible to increase the layout modularity by enforcing symmetry constraints in (4). A straightforward way to achieve modularity is to use the Mth order rotational symmetry, as applied in [21], for which only the element locations in a slice of $2\pi/M$ radians are optimizated and the "optimal" slice is periodically repeated M times in a rotationally symmetric layout. Interested readers are referred to [22] for a detailed discussion on quasi-modular aperiodic arrays with rotational symmetry. With layout modularity, we refer to the rotational symmetry in the rest of this article.

The optimization problem in (4) is a convex, and namely a second-order cone programming problem [23], which can be efficiently solved using the interior point method based solvers in CVX [24]. The comparative examples in [10] clearly show the superior performance of the technique applied in this article as compared to the relevant alternatives available in the literature. Moreover, considering its practical interest and further SLL suppression capability, a phase optimization [25] can be added to the already optimized positioning (at the expense of some power efficiency loss), which is not considered in this article.

Next, the settings used for the optimization (in MATLAB) are listed as follows.

1) Sector definition: ± 60 / $\pm 15^\circ$ in azimuth/elevation [5]. In this article, we aim to minimize the maximal SLL within the sector. If required by the application, the optimization routine can easily be modified for SLL minimization for the whole visible region.
2) Number of elements, $N = 64$ ($r = 0.28$) or 256 ($r = 0.13$).
3) Initial array layout is 8 by 8 or 16 by 16, periodic, 0.5λ-spaced square grid array.
4) Element pattern, $E_n = \cos\theta$ (common embedded pattern). With increased computational demands, it is also possible to include mutual coupling in the topology optimization procedure via embedded pattern simulations as demonstrated in [26] and [27]. In this article, for simplicity, we used a cosine-shaped embedded pattern for all the elements as an approximation.
5) Operation frequency, $f_0 = 28$ GHz.
6) Minimum element spacing, $d_{\min} = 0.5\lambda$ or 1λ.
7) Enforced symmetry, when applied, is rotational with $M = 4$.
8) Upper bound for the position perturbations, $\mu = 0.08\lambda$ (exhibits stable and fast convergence [10]).
9) Number of scan positions, $S = 9$, including 1 beam at broadside (i.e. $u_s = v_s = 0$), four beams at the corners of the sector (i.e., $u_s = \pm 60^\circ$, $v_s = \pm 15^\circ$) and four beams at the centers of the sector edges (i.e., $u_s = \pm 60^\circ$, $v_s = 0$ and $u_s = 0$, $v_s = \pm 15^\circ$), which effectively covers the whole scan range and ensures that for the result of the cost function is maintained for a beam scanned freely inside the given sector.

Due to the increased computational demands with the larger arrays with 256 elements, the optimizations in this part have been carried out in TU Delft's 32-processor Intel(R) Xeon(R) CPU E5-2650 v2 at 2.60 GHz 128 GB RAM Red Hat Enterprise Linux Server.

It is worth of note that the layout optimization strategy used in this article is based on minimizing the side lobes (thus, the interuser interference), while serving the intended user with a single-lobe beam toward the user position (in the case of a line-of-sight (LoS) communication), or toward the direction of the strongest multipath component of the user (in the case of a non-line-of-sight (NLoS) communication) [28], [29]. Such a strategy can be considered as the "traditional" approach, as the maximization of directivity and minimization of average SLL yields the optimal quality-of-service (QoS). However, it is useful to mention that recent works in [30] and [31] proposed the possibility to consider the QoS as a driving aspect in the array design process, which leads to a new "capacity-oriented" design methodology.

B. Communication System Aspects

This section considers the use-case scenario and user selection and beamforming strategies for the evaluation of the QoS performance and processing complexity of the proposed optimal array topologies.

We consider an isolated cell in a pure LoS environment in which a base station with N-antenna elements is serving K single, omnidirectional antenna users simultaneously in the same narrow frequency subband using space division multiple access (SDMA) [1]. The other subbands can potentially be occupied by K', K'', etc., users at the same time. Table II provides the nomenclature used in the system model [32].

Following the notation given in Table II, the precoded signal vector $\boldsymbol{x} \in \mathbb{C}^{N\times 1}$ is given by

$$\boldsymbol{x} = \boldsymbol{W}\boldsymbol{q} \quad (5)$$

where $\boldsymbol{W} \in \mathbb{C}^{N\times K}$ is the precoding matrix and $\boldsymbol{q} \in \mathbb{C}^{K\times 1}$ is the input signal vector.

Then, the received signal vector $\boldsymbol{y}$ is expressed as

$$\boldsymbol{y} = \sqrt{\boldsymbol{\rho}} \cdot (\boldsymbol{H}\boldsymbol{x}) + \boldsymbol{n} \quad (6)$$

TABLE II
NOMENCLATURE USED IN THE SYSTEM MODEL [32]

Notation	Description
$\boldsymbol{q} \in C^{K\times 1}$	Input signal vector at the base station ($\{\|q_k\|^2\}=1$)
$\boldsymbol{W} \in C^{N\times K}$	Precoding matrix ($\sum_{n=1}^{N}\|W_{n,k}\|^2=1$ for $\forall k \in \{1,\ldots,K\}$)
$\boldsymbol{x} \in C^{N\times 1}$	Precoded signal vector transmitted from the base station antenna
$\boldsymbol{n} \in C^{K\times 1}$	Unit-variance Additive White Gaussian Noise (AWGN)
$\boldsymbol{\rho} \in C^{K\times 1}$	Vector proportional to the maximal SNRs at the users
$\boldsymbol{H} \in C^{K\times N}$	Channel matrix ($\{\|H_{k,n}\|^2\}=1$)
$\boldsymbol{y} \in C^{K\times 1}$	Received signal vector at the users
$\boldsymbol{P} \in C^{K\times 1}$	Average adaptive transmit power allocated to the users

where $\boldsymbol{H} \in \mathbb{C}^{K\times N}$ is the channel matrix and $\boldsymbol{n} \in \mathbb{C}^{K\times 1}$ is the noise vector.

The entries of the channel matrix $\boldsymbol{H}$ are formulated as [33]

$$H_{k,n} = \beta_{k,n} G_n(\hat{r}_{kn}) \frac{e^{-j\frac{2\pi}{\lambda}|r_k - r_n|}}{|r_k - r_n|} \tag{7}$$

where $G_n(\hat{r}_{kn})$ is the far-field function of the nth base station antenna element in the direction $\hat{r}_{kn}$, from the nth element towards the kth user. $|r_k - r_n|$ ($\approx |r_k|$) is the distance between the nth element and the kth user. $\beta_{k,n}$ is the normalization constant. For simplicity, let us assume a common embedded element pattern, $G(\hat{r}_k) = G_n(\hat{r}_{kn}),\ \ \forall n \in \{1,\ldots,N\}$.

As a result, the downlink SINR for the kth user is given by

$$\text{SINR}_k = \frac{\rho_{k;k}|\boldsymbol{H}_{k,:}\boldsymbol{W}_{:,k}|^2}{\sum_{j\neq k}^{K}\rho_{k;j}|\boldsymbol{H}_{k,:}\boldsymbol{W}_{:,j}|^2 + 1} \tag{8}$$

where $\rho_{k;j}$ is calculated as

$$\rho_{k,j}(dB) = P_j(dBm) - 20\log_{10}[f_0] - 20\log_{10}\left[\frac{4\pi}{c}\right] - 20\log_{10}[|\boldsymbol{r}_k|] + G(\hat{\boldsymbol{r}}_k)(dB) - N_{th}(dBm) \tag{9}$$

where P_j is the average adaptive transmit power to the jth user with equalized signal-to-noise ratio (SNR), c is the speed of light and N_{th} is the thermal noise power.

For the precoding, we exploit the two commonly applied techniques: conjugate beamforming (CB) and zero forcing (ZF) [32]. The generalized (LoS/NLoS) precoding matrix $\boldsymbol{W}$ for the two techniques is given by

$$\boldsymbol{W} = \begin{cases} \boldsymbol{H}^{\dagger} & \text{for CB} \\ \boldsymbol{H}^{\dagger}(\boldsymbol{H}\boldsymbol{H}^{\dagger})^{-1} & \text{for ZF} \end{cases} \tag{10}$$

where † denotes the Hermitian transpose.

Later, in Section III-B, the statistical system QoS performance evaluation (in MATLAB) is given in terms of the cumulative distribution function (CDF) of SINR at the user ends, while the computational cost is given in terms of floating point operations per second (FLOPS). According to [34], the number of FLOPS in the case of CB ($\#\mathcal{F}_{\text{CB}}$) and ZF ($\#\mathcal{F}_{\text{ZF}}$) is given by

$$\#\mathcal{F}_{\text{CB}} = K(14N - 2) \tag{11}$$

$$\#\mathcal{F}_{\text{ZF}} = K(24(K-1)N^2 + 48(K-1)^2N + 54(K-1)^3 + 6N) \tag{12}$$

The simulation parameters used in the system studies are summarized in Table III.

TABLE III
COMMUNICATION SYSTEM SIMULATION PARAMETERS

Center frequency (GHz)	28
Number of array elements at the base station	64, 256
Number of simultaneous co-frequency users	4, 8
Maximal communication range (m)	200
Maximal per-user SNR (dB)	20, 25
Minimum angular spacing between users (in uv-plane)	0.28, 0.13
Number of random user location realizations	10,000

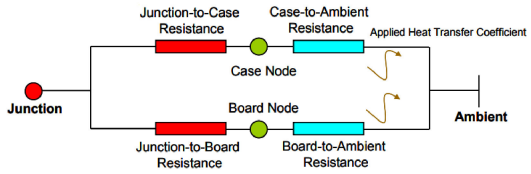

Fig. 1. Two-resistor compact thermal model [37].

The users' locations are randomly selected from uniformly distributed points in the uv-plane (within the ± 60 by $\pm 15^{\circ}$ window), using the interference-aware (i.e., with well-separated user beams) scheduling algorithm proposed in [1]. For comparison, we use two different minimum angular separation conditions (= 1/(Array Length in λ) units in the uv-plane) between the users, which are suitable for arrays larger in size than a $\lambda/2$-spaced 8-by-8 and a 16-by-16 reference antennas. Furthermore, we apply adaptive power transmission with equalized SNRs and for comparison, we consider two different maximal peruser SNR values (achieved only with a uniformly fed array with progressive phase shifts) that are in line with the currently proposed 5G link budgets in the literature [35], [36]. It is worthy of note that we assume the user-dependent path losses, impedance matching performance of the antennas, and scanning losses are taken into account in the transmission power control so that the maximal SNR of each user is kept fixed and the main focus of the study remains as the investigation of the antenna array topology impact on the interference.

C. Thermal Aspects

The modeling approach and settings for the thermal simulations (performed in CST Studio Suite—MultiPhysics, CST MPS) are listed as follows.

1) *Simulation model:* Two-resistor compact thermal model [37]. The model for a single chip is as given in Fig. 1.
2) *Cooling strategy:* Passive-only cooling (natural convection and radiation) with a nonfinned flat plate.
3) *Design strategy:* A double-sided design (two substrates supporting patches and ICs on opposite sides, with a ground plane in between), one IC per element [14].
4) Heat per element is directly proportional (with a constant 1) to the RF power required for multiple users.
5) *Board properties:* Same material and size in all topologies for fair comparison. Two design concepts are used: (i) conventional antenna (i.e., with a thin ground plane), (ii) planar heatsink antenna (i.e., with a thick ground plane and extended board edge length) [38].

A list of thermal simulation parameters is given in Table IV.

TABLE IV
THERMAL MODEL PARAMETERS

Heat produced per element (W)	2 (for N = 64) [8] 0.125 (for N = 256)
Patch / IC board material	Rogers RT5880
Patch / IC board thickness (mm)	0.508
Ground plane thickness, t_g (mm)	0.05 (thin) / 2 (thick)
Board edge length, L_b (λ)	12 (for t_g = 0.05 mm) 20 (for t_g = 2 mm)
Chip dimensions (mm)	3 x 3 x 0.5
IC junction-to-case resistance (W/K) [14]	10
IC junction-to-board resistance (W/K) [14]	15
Heat transfer coefficient at the air interfaces (W/m^{2}K) [37]	10
Surface emissivity	0.9
Ambient temperature (^{o}C)	25

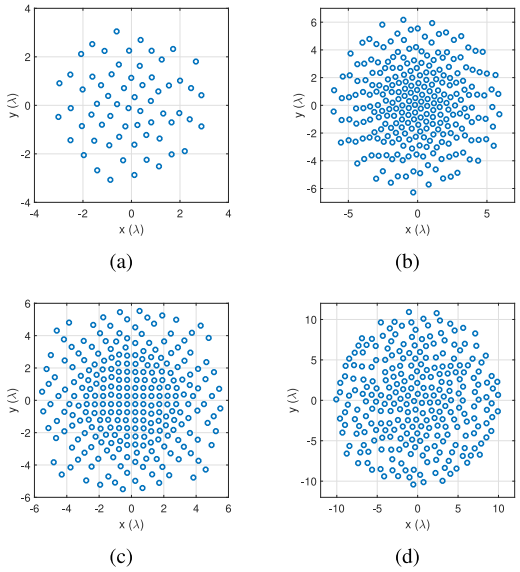

Fig. 2. Optimal aperiodic array layouts: (a) 64-element, fully aperiodic, $d_{\min} = 0.5\lambda$, (b) 256-element, fully aperiodic, $d_{\min} = 0.5\lambda$, (c) 256-element, quasi-modular, $d_{\min} = 0.5\lambda$, and (d) 256-element, fully aperiodic, $d_{\min} = 1\lambda$.

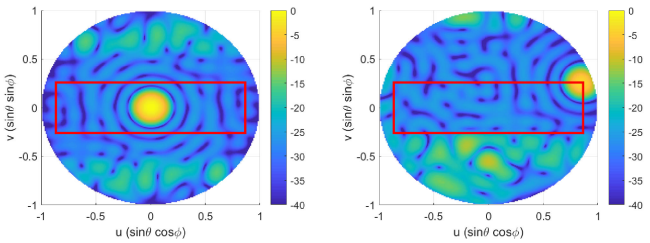

Fig. 3. Radiation pattern at f_0 (normalized w.r.t. broadside gain, in dB) of the 64-element, fully aperiodic array with $d_{\min} = 0.5\lambda$. (a) broadside beam and (b) corner beam.

III. SIMULATION RESULTS

A. Electromagnetic Aspects

Using the optimization routine and settings in Section II-A, the following four different array topologies have been synthesized:

i) 64-element, fully aperiodic, $d_{\min} = 0.5\lambda$ (layout is provided in Fig. 2(a), radiation pattern is shown in Fig. 3);

ii) 256-element, fully aperiodic, $d_{\min} = 0.5\lambda$ (layout is provided in Fig. 2(b), radiation pattern is shown in Fig. 4);

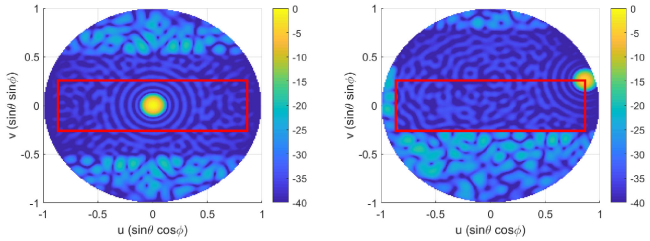

Fig. 4. Radiation pattern at f_0 (normalized w.r.t. broadside gain, in dB) of the 256-element, fully aperiodic array with $d_{\min} = 0.5\lambda$: (a) broadside beam and (b) corner beam.

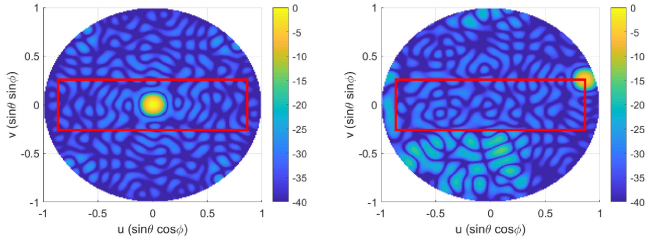

Fig. 5. Radiation pattern at f_0 (normalized w.r.t. broadside gain, in dB) of the 256-element, quasi-modular array with $d_{\min} = 0.5\lambda$: (a) broadside beam and (b) corner beam.

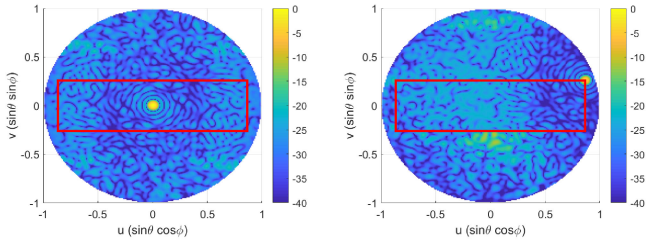

Fig. 6. Radiation pattern at f_0 (normalized w.r.t. broadside gain, in dB) of the 256-element, fully aperiodic array with $d_{\min} = 1\lambda$: (a) broadside beam and (b) corner beam.

TABLE V
MAXIMAL IN-SECTOR SLLS (WITH RESPECT TO THE FIELD STRENGTH AT BROADSIDE) AND ARRAY DIRECTIVITIES FOR MULTIPLE STEERABLE BEAMS WITHIN THE SECTOR

Array topology	Maximal SLL (dB)	Broadside beam directivity (dBi)	Corner beam directivity (dBi)
64-element, periodic, 0.5λ-spaced	-12.8	23.0	20.4
64-element, fully aperiodic, $d_{\min}$ = 0.5λ	-25.2	24.4	20.1
256-element, periodic, 0.5λ-spaced	-13.2	29.1	25.7
256-element, fully aperiodic, $d_{\min}$ = 0.5λ	-33.4	29.7	25.7
256-element, quasi-modular, $d_{\min}$ = 0.5λ	-28.1	30.2	25.5
256-element, fully aperiodic, $d_{\min}$ = 1λ	-22.3	30.7	26.0

iii) 256-element, quasi-modular, $d_{\min} = 0.5\lambda$ (layout is provided in Fig. 2(c), radiation pattern is shown in Fig. 5);

iv) 256-element, fully aperiodic, $d_{\min} = 1\lambda$ (layout is provided in Fig. 2(d), radiation pattern is shown in Fig. 6).

The maximal SLL at f_0 (with respect to the array's broadside field strength) for each topology is given in Table V, in which the broadside (and corner beam) directivity is the numerically computed directivity of the array [39] when the main beam is at $u = v = 0$ (and $u = \sin 60^o$, $v = \sin 15^o$). Fig. 7 provides the cost function (i.e., maximal in-sector SLL) evolution within the

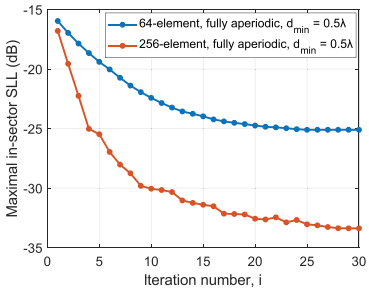

Fig. 7. Evolution of the maximal SLL within the sector for the synthesized 64- and 256-element fully aperiodic arrays within the iterative optimization routine presented in Section II-A.

iterative optimization routine for the two fully aperiodic arrays in Case (i) and Case (ii).

From the results, the following main observations have been made.

1) Aperiodic arrays provide much better maximal SLL suppression than the periodic counterparts (reduction from -13.2 to -25.2 dB for 64-elements).

2) As compared to the 64-element counterpart, the 256-element aperiodic array has much better SLL suppression capability (reduction from -25.2 to -33.4 dB).

3) Applying layout modularity (to have design and calibration simplification) causes an increase in the peak SLL (from -33.4 dB for no symmetry to -28.1 dB for fourth order rotational symmetry with 256 elements).

4) Increasing the minimum interelement distance (to have extra physical space for the ICs and feeding lines, to provide extra cooling as will be seen in Section III-C) has a significant impact on the maximal SLL (increase from -33.4 dB for $d_{\min} = 0.5\lambda$ to -22.3 dB for $d_{\min} = 1\lambda$ with 256 elements).

Note that the maximal SLL values given in Table V can only be maintained over a narrow bandwidth, since the topology optimization is performed at a single frequency. The effect of operation bandwidth on the irregular array pattern results is visualized in Fig. 8, for which the corner beam radiation pattern of the 256-element, fully aperiodic array with $d_{\min} = 0.5\lambda$ at the design frequency f_0 is taken as the reference [see Fig. 4(b)]. It is seen that, due to the scaling of the array (in terms of λ):

i) decreasing the operating frequency increases the beamwidth. Therefore, it will be necessary to increase the minimum angular spacing between the simultaneous cofrequency users to maintain a high QoS.

ii) increasing the frequency leads to the appearance of high side lobes in the field-of-view, which will deteriorate the statistical QoS.

In mm-wave 5G applications, the relative bandwidth is narrow and the impact of the array scaling on the pattern is not so significant. For example, the $f_0 = 28$-GHz *n257* 5G NR frequency band extends from 26.5 ($0.95f_0$) to 29.5 GHz ($1.05f_0$). Similar figures are obtained in other 5G mm-wave bands (such as *n258, n260, n261*) as well.

For broadband applications, on the other hand, the algorithm in [10] (which is what we used in this article) can be straightforwardly extended to a multifrequency multibeam

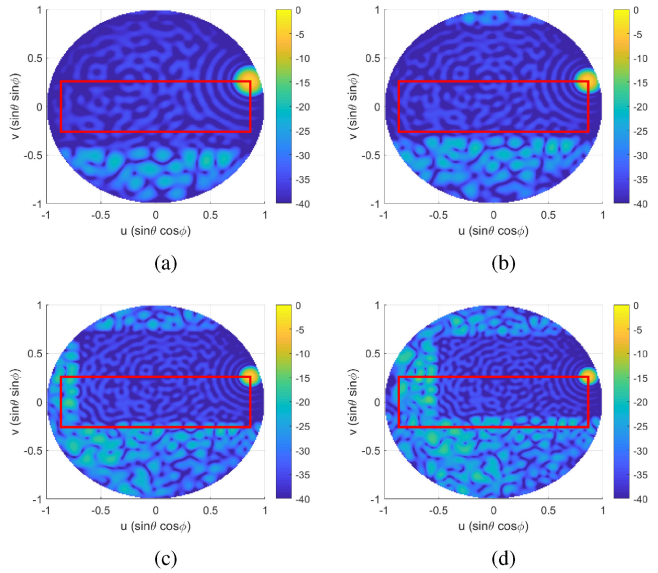

Fig. 8. Corner beam radiation pattern (normalized w.r.t. broadside gain, in dB) of the 256-element, fully aperiodic array with $d_{\min} = 0.5\lambda$ at different operating frequencies: (a) $0.75f_0$, (b) $0.9f_0$, (c) $1.1f_0$, and (d) $1.25f_0$.

TABLE VI
MINIMAL SINR (STATISTICALLY ACHIEVED FOR MORE THAN 95% OF TOTAL OCCURRENCES) FOR EIGHT SIMULTANEOUS COFREQUENCY USERS WITH MINIMUM uv-PLANE ANGULAR SPACING OF 0.28 UNITS AND MAXIMAL PER USER SNR OF 20 dB, CORRESPONDING TO FIG. 9(C)

Array topology & precoding strategy	Minimal SINR (dB)
64-element, periodic, 0.5λ-spaced, CB	7.9
64-element, fully aperiodic, $d_{\min}$ = 0.5λ, CB	14.0
64-element, periodic, 0.5λ-spaced, ideal ZF	19.6
256-element, periodic, 0.5λ-spaced, CB	14.2
256-element, fully aperiodic, $d_{\min}$ = 0.5λ, CB	18.4
256-element, periodic, 0.5λ-spaced, ZF	19.9
256-element, quasi-modular, $d_{\min}$ = 0.5λ, CB	17.1
256-element, fully aperiodic, $d_{\min}$ = 1λ, CB	13.0

peak SLL minimization tool, as done in [40]. Depending on the desired bandwidth, such an optimization would yield higher SLL than the ones reported in Table V. However, the achieved level would be preserved over a wider range of frequencies.

B. Communication System Aspects

This section relates the radiation pattern results of different array topologies and precoding strategies to the system's QoS statistically. Using the settings in Section II-B, the communication system simulations have been performed.

Figs. 9 and 10 show the CDF of SINR for 4/8 simultaneous cofrequency users with 20/25 dB maximal SNR per user, when the minimum distance between the users in the uv-plane is equal to 0.28 and 0.13 units, respectively. For more insight, note that at the maximal communication range of 200 m, for users located at a similar height with the base station near its broadside, the uv-plane user separation of 0.28 and 0.13 units corresponds to approximately 56 and 26 m, respectively. The formulation of conversion between the Cartesian and uv-plane coordinates can be found in [1].

Corresponding to Figs. 9(c) and 10(c), Tables VI and VII exemplifies the minimal SINR attained in 95% of the total occurrences, with eight users and 20 dB maximal per-user SNR,

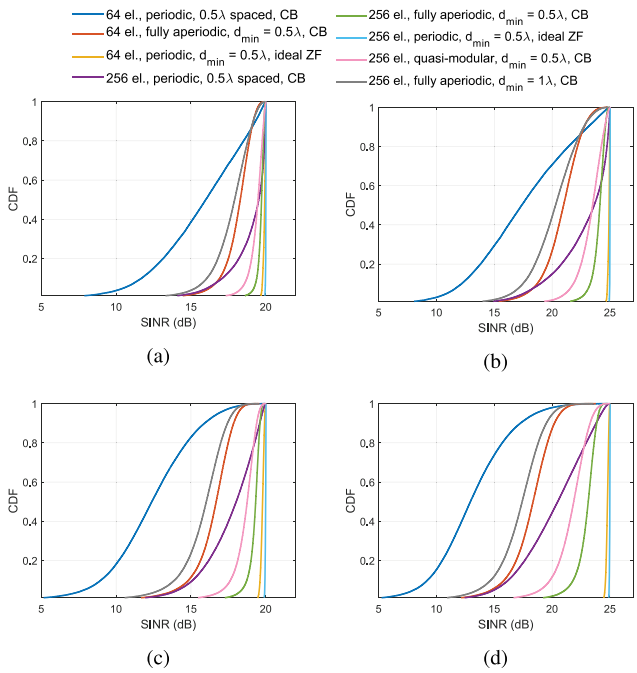

Fig. 9. CDF of SINR for different array topologies and precoding strategies for the minimum interuser uv-plane distance of 0.28 units, with: (a) 4 SDMA users and 20 dB maximal SNR per user, (b) 4 SDMA users and 25 dB maximal SNR per user, (c) 8 SDMA users and 20 dB maximal SNR per user, and (d) 8 SDMA users and 25 dB maximal SNR per user.

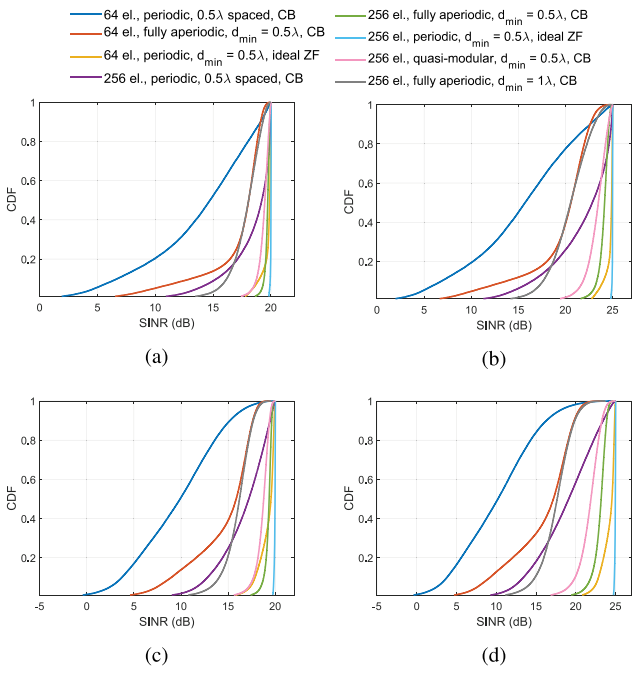

Fig. 10. CDF of SINR for different array topologies and precoding strategies for the minimum interuser uv-plane distance of 0.13 units, with: (a) 4 SDMA users and 20 dB maximal SNR per user, (b) 4 SDMA users and 25 dB maximal SNR per user, (c) 8 SDMA users and 20 dB maximal SNR per user, and (d) 8 SDMA users and 25 dB maximal SNR per user.

TABLE VII
MINIMAL SINR (STATISTICALLY ACHIEVED FOR MORE THAN 95% OF TOTAL OCCURRENCES) FOR EIGHT SIMULTANEOUS COFREQUENCY USERS WITH MINIMUM uv-PLANE ANGULAR SPACING OF 0.13 UNITS AND MAXIMAL PER USER SNR OF 20 dB, CORRESPONDING TO FIG. 10(C)

Array topology & precoding strategy	Minimal SINR (dB)
64-element, periodic, 0.5λ-spaced, CB	2.4
64-element, fully aperiodic, $d_{\min}$ = 0.5λ, CB	7.4
64-element, periodic, 0.5λ-spaced, ideal ZF	17.3
256-element, periodic, 0.5λ-spaced, CB	11.6
256-element, fully aperiodic, $d_{\min}$ = 0.5λ, CB	18.5
256-element, periodic, 0.5λ-spaced, ZF	19.8
256-element, quasi-modular, $d_{\min}$ = 0.5λ, CB	17.2
256-element, fully aperiodic, $d_{\min}$ = 1λ, CB	13.1

for the minimum interuser uv-plane distance of 0.28 and 0.13 units, respectively.

The performance of a 64-element (8-by-8) periodic (square-grid) array with $d_{\min} = 0.5\lambda$ using ZF (i.e., ideally with no interbeam interference) has been taken as the benchmark here.

From the simulation results (with the statistical criterion of 95% [41]), the following main observations have been made.

1) As the exact information of the channel is practically not known and CB can be applied more reliably in most of the cases instead of ZF, fully aperiodic arrays provide significant SINR improvements as compared to their periodic counterparts. For example, Tables VI and VII show around 6 dB (for 64 elements) and 4 dB (for 256 elements) increase in the minimal SINR in the case of minimal angular spacing of 0.28 units and 5 and 7 dB for 64 and 256 elements correspondingly) in the case of minimal angular spacing of 0.13 units.

2) The 256-element periodic/aperiodic arrays with CB/ZF provides much better statistical QoS as compared to their 64-element counterparts, thanks to their higher beam resolution. In the periodic topology, for the minimal user spacing of 0.28 units, the far side lobes (which are much lower than the first side lobe) of the 256-element array become the major source of interference. In line with this reasoning, Fig. 9 shows that the 256-element periodic array can achieve even a slightly better statistical QoS performance than the 64-element fully irregular array. For the minimal user spacing of 0.13 units, the 64-element array cannot resolve two users with an angular separation less than 0.28 units, which causes a significant reduction in the QoS as compared to that of a 256-element array (see Fig. 10).

TABLE VIII
COMPARISON OF COMPUTATIONAL COST IN PRECODING

Number of elements at the base station array, N	Number of simultaneous co-frequency users, K	Precoding strategy	Number of FLOPS
64	4	CB	3576
64	8	CB	7152
64	4	ZF	1297608
64	8	ZF	6860496
256	4	CB	14328
256	8	CB	28656
256	4	ZF	19328712
256	8	ZF	93057744

3) The 256-element fully aperiodic array with CB achieves a close statistical QoS to the one of the reference case (i.e., 64-element periodic array with ideal ZF). The minimal SINR is even higher (by 1.2 dB) for the irregular 256-element array with CB as compared to the reference in one study case given in Fig. 10(c) and Table VII. Since this performance is achieved with CB instead of ZF (thanks to the large-scale aperiodic layout), the QoS becomes more robust against channel impurities [42].

4) In addition to the previous point, the use of large-scale aperiodic arrays with CB can help decrease the computational burden of precoding significantly when compared to the reference array with 64-elements applying ZF. Table VIII provides a comparison of computational cost in precoding in terms of the

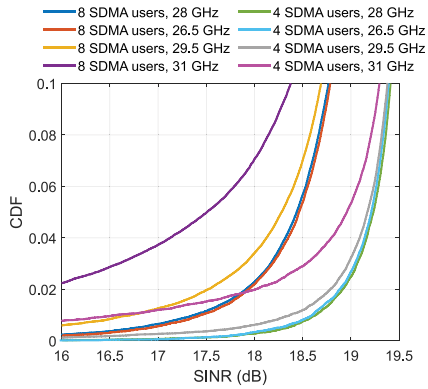

Fig. 11. CDF of SINR at different frequency subbands for the minimum interuser uv-plane distance of 0.13 units and maximal peruser SNR of 20 dB with the 256-element, fully aperiodic, $d_{\min} = 0.5\lambda$ array under CB precoding.

total number of FLOPS given in (11) and (12). By taking the $N = 64$, $K = 4$ and 8, ZF cases as reference, it can be computed that the $N = 256$-element array under CB yields only 1.1% and 0.4% of the total number of FLOPS of the reference for 4 and 8 users, respectively.

5) Introducing layout modularity or increasing the sparsity in the 256-element arrays causes a decrease in the QoS with CB. The effect is relatively small when changing from the fully aperiodic to the quasimodular array with $d_{\min} = 0.5\lambda$ (1.3 dB reduction is seen in Tables VI and VII). The impact on statistical SINR is more serious for the array with $d_{\min} = 1\lambda$ (5.4 dB reduction is seen in Tables VI and VII), which shifts the SINR curve just behind/ahead of that of the 256-element periodic CB-precoded array with $d_{\min} = 0.5\lambda$ in Fig 9/Fig. 10.

6) Since we assume that the maximal SNR per user is fixed, increasing the number of users results in increased power demand. Besides, the total interference level increases (with the QoS decreasing accordingly) with the number of users. The effect is more visible for the periodic arrays when compared to the aperiodic ones due to the relatively higher side lobes in the regular topologies. For example, by comparing Fig. 10(a) and (c), it is seen that the minimal SINR statistically achieved for more than 95% of total occurrences is 2.1 and 0.8 dB higher for 4 users as compared to the 8 user case in the case of using the 256-element, periodic, 0.5λ-spaced array with CB and the 256-element, fully aperiodic, $d_{\min} = 0.5\lambda$ array with CB, respectively.

Next, the impact of bandwidth on the statistical SINR results is studied. Fig. 11 shows the CDF of SINR curves (zoomed in to the region-of-interest) at different frequency subbands for the 256-element, fully aperiodic, $d_{\min} = 0.5\lambda$ array under CB precoding in the case of interuser uv-plane separation of 0.13 units and maximal per-user SNR of 20 dB. In line with the results in Fig. 8, it is seen that the statistical SINR performance is very stable within the 5G NR band (*n257* mm-wave band: 26.5–29.5 GHz is taken as an example). The statistical QoS degrades if the optimized array is used beyond that range. The SINR performance at the 31 GHz subband is shown on Fig. 8 as an example. As already mentioned in Section III-A, such broadband applications would require a multibeam array which is jointly optimized for multiple frequencies in a wide range [40].

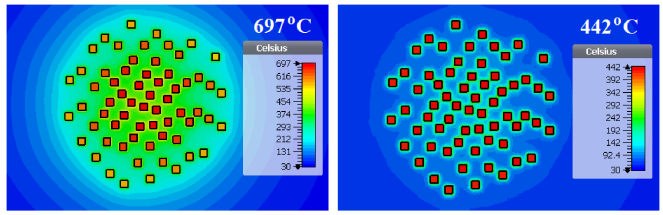

(a) (b)

Fig. 12. IC temperature distribution in the 64-element, fully aperiodic array with $d_{\min} = 0.5\lambda$: (a) conventional antenna: $L_b = 12\lambda$ and $t_g = 0.05$ mm and (b) heatsink antenna: $L_b = 20\lambda$ and $t_g = 2$ mm.

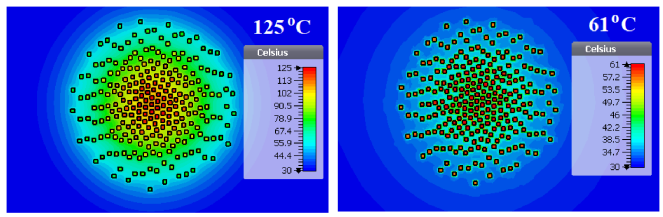

(a) (b)

Fig. 13. IC temperature distribution in the 256-element, fully aperiodic array with $d_{\min} = 0.5\lambda$: (a) conventional antenna: $L_b = 12\lambda$ and $t_g = 0.05$ mm and (b) heatsink antenna: $L_b = 20\lambda$ and $t_g = 2$ mm.

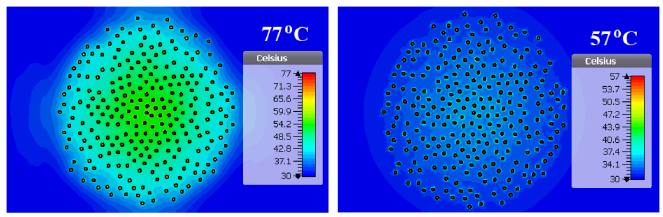

(a) (b)

Fig. 14. IC temperature distribution in the 256-element, fully aperiodic array with $d_{\min} = 1\lambda$: (a) conventional antenna: $L_b = 12\lambda$ and $t_g = 0.05$ mm and (b) heatsink antenna: $L_b = 20\lambda$ and $t_g = 2$ mm.

C. Thermal Aspects

Last, thermal simulations have been performed for the following three selected topologies:

i) 64-element, fully aperiodic, $d_{\min} = 0.5\lambda$ [see Fig. 2(a)];
ii) 256-element, fully aperiodic, $d_{\min} = 0.5\lambda$ [see Fig. 2(b)];
iii) 256-element, fully aperiodic, $d_{\min} = 1\lambda$ [see Fig. 2(c)].

For the two design approaches (namely the conventional antenna, with $t_g = 0.05$ mm and the heatsink antenna, with $t_g = 2$ mm, as described in Section II-C), using the settings as previously listed in Table IV. Note that the 25 °C ambient temperature setting is an optimistic assumption that will not apply to some countries in summertime. Therefore, if any, the relative difference in the ambient temperature should be added to the given simulation results for correct evaluation of the thermal performance under different environmental conditions.

The temperature distributions for the three cases are shown in Figs. 12–14, respectively. Note that the figures are zoomed-in to the array centers. Table IX summarizes the outcome. From the results, the following main conclusions have been drawn.

1) Due to the extremely large heat per element, the 64-element layout results in unacceptably high IC temperatures. This clearly

TABLE IX
MAXIMAL IC JUNCTION TEMPERATURES (WITH CONSTANT EIRP)

Array topology	Maximal temperature (^oC)
64-element, fully aperiodic, $d_{\min} = 0.5\lambda$, conventional antenna	697
64-element, fully aperiodic, $d_{\min} = 0.5\lambda$, heatsink antenna	442
256-element, fully aperiodic, $d_{\min} = 0.5\lambda$, conventional antenna	125
256-element, fully aperiodic, $d_{\min} = 0.5\lambda$, heatsink antenna	64
256-element, fully aperiodic, $d_{\min} = 1\lambda$, conventional antenna	77
256-element, fully aperiodic, $d_{\min} = 1\lambda$, heatsink antenna	57

shows that using a single nonfinned flat plate is not sufficient for cooling of such arrays, and there must be a big finned heatsink behind the radiators for passive-only cooling [8], [14].

2) For the same EIRP requirement with the 64-element array, the 256-element topology (with $d_{\min} = 0.5\lambda$) can bring the temperature down to the edge of the acceptable limit of 125 °C [43] with the conventional antenna, under the current settings. Using a heatsink antenna design can provide additional passive cooling, which yields a maximal IC temperature of 64 °C.

3) The sparse 256-element topology (with $d_{\min} = 1\lambda$) can provide a safe temperature (77 °C), even with the conventional design (i.e., with a low equivalent thermal conductivity board). The temperature can be further decreased (up to 57 °C) by using a more complex heatsink antenna design employing a thick ground plane.

IV. CONCLUSION

Novel large-scale (256-element) aperiodic multibeam arrays have been proposed to be used in the future 5G/6G base stations. Adding more elements into the design has allowed to achieve more gain and much lower side lobes; thus much less power and less heat generation per element with more surface for cooling. This brings the following key system advantages of the proposed arrays over the existing/discussed periodic/aperiodic 64-element antennas.

1) The electricity consumption is reduced remarkably.

2) A similar statistical QoS performance to the one of the ideal ZF is achieved by using CB precoding, which significantly decreases the computational complexity (to less than 1% of ZF) and increases the robustness against the operation bandwidth and the nonideal system conditions (such as channel impurities, quantization errors, estimation errors, etc.).

3) Fully passive cooling (via natural convection and thermal radiation) to a safe and reliable maximal IC temperature is achieved by using a single, nonfinned, flat antenna/IC board, with no additional finned heatsink behind the array.

4) The layout sparsity can be much increased (to provide more space for the electronics, or to enhance the passive cooling capacity), with only limited impact on the QoS statistically.

Apart from the apparent increase in the (RF) hardware (but without the massive thermal hardware with the fins of existing designs), the price to pay is the increased design/fabrication complexity (with irregular IC feeding and routing), and calibration requirements. This can be partially compensated by enforcing (quasi-) modularity in the synthesis procedure, which comes with some compromise against the SLL suppression capability.

REFERENCES

[1] Y. Aslan, J. Puskely, A. Roederer, and A. Yarovoy, "Trade-offs between the quality of service, computational cost and cooling complexity in interference-dominated multi-user SDMA systems," *IET Comm.*, vol. 14, no. 1, pp. 144–151, Jan. 2020.

[2] E. McCune, "Fundamentals for energy-efficient massive MIMO," in *Proc. IEEE Wireless Commun. Netw. Conf. Workshops*, San Francisco, CA, USA, Mar. 2017, pp. 1–6.

[3] B. J. Döring, "Cooling system for a ka band transmit antenna array," German Aerospace Center (DLR), Köln, Germany, Tech. Rep. IB554-06/02, Dec. 2005.

[4] P. Wongchampa and M. Uthansakul, "Orthogonal beamforming for multiuser wireless communications: Achieving higher received signal strength and throughput than with conventional beamforming," *IEEE Antennas Propag. Mag.*, vol. 59, no. 4, pp. 38–49, Jun. 2017.

[5] E. Degirmenci, "Emf test report: Ericsson AIR 5121," Ericsson AB, Stockholm, Sweden, Tech. Rep. GFTB-17:001589 Uen Rev B, Jan. 2018.

[6] R. Valkonen, "Compact 28-GHz phased array antenna for 5G access," in *Proc. IEEE/MTT-S IMS*, Philadelphia, PA, USA, Jun. 2018, pp. 1334–1337.

[7] B. Sadhu *et al.*, "A 28 GHz 32-element phased-array transceiver IC with concurrent dual polarized beams and 1.4 degree beam-steering resolution for 5G communication," in *Proc. IEEE Int. Solid-State Circuits Conf.*, San Francisco, CA, USA, Feb. 2017, pp. 128–129.

[8] Y. Aslan, C. E. Kiper, A. J. van den Biggelaar, U. Johannsen, and A. Yarovoy, "Passive cooling of mm-wave active integrated 5G base station antennas using CPU heatsinks," in *Proc. 16th EuRAD*, Paris, France, Oct. 2019, pp. 121–124.

[9] Y. Wang *et al.*, "A 39 GHz 64-element phased-array CMOS transceiver with built-in calibration for large-array 5G NR," in *Proc. IEEE RFIC Symp.*, 2019, pp. 247–250.

[10] Y. Aslan, J. Puskely, A. Roederer, and A. Yarovoy, "Multiple beam synthesis of passively cooled 5G planar arrays using convex optimization," *IEEE Trans. Antennas Propag.*, vol. 68, no. 5, pp. 3557–3566, May 2020.

[11] P. Rocca, G. Oliveri, R. J. Mailloux, and A. Massa, "Unconventional phased array architectures and design methodologies—A review," *Proc. IEEE*, vol. 104, no. 3, pp. 544–560, Mar. 2016.

[12] G. Oliveri *et al.*, "Codesign of unconventional array architectures and antenna elements for 5G base stations," *IEEE Trans. Antennas Propag.*, vol. 65, no. 12, pp. 6752–6767, Dec. 2017.

[13] Y. Aslan, J. Puskely, A. Roederer, and A. Yarovoy, "Effect of element number reduction on inter-user interference and chip temperatures in passively-cooled integrated antenna arrays for 5G," in *Proc. 14th EuCAP*, Copenhagen, Denmark, Mar. 2020.

[14] Y. Aslan, J. Puskely, J. H. J. Janssen, M. Geurts, A. Roederer, and A. Yarovoy, "Thermal-aware synthesis of 5G base station antenna arrays: An overview and a sparsity-based approach," *IEEE Access*, vol. 6, pp. 58 868–58 882, 2018.

[15] E. McCune, "Energy efficiency maxima for wireless communications: 5G, IoT, and massive MIMO," in *Proc. IEEE China Int. Capital Corp.*, Austin, TX, USA, May 2017.

[16] B. Steinberg, "The peak sidelobe of the phased array having randomly located elements," *IEEE Trans. Antennas Propag.*, vol. AP-20, no. 2, pp. 129–136, Mar. 1972.

[17] Y. T. Lo, "A mathematical theory of antenna arrays with randomly spaced elements," *IEEE Trans. Antennas Propag.*, vol. AP-12, no. 3, pp. 257–268, May 1964.

[18] G. Buonanno and R. Solimene, "Comparing different schemes for random arrays," *Prog. Electromagn. Res. B*, vol. 71, pp. 107–118, 2016.

[19] Anokiwave Inc., "Anokiwave introduces 5G mmW reconfigurable 256-element active antenna array," Press Release, Oct. 2017.

[20] B. Fuchs, A. Skrivervik, and J. R. Mosig, "Synthesis of uniform amplitude focused beam arrays," *IEEE Antennas Wireless Propag. Lett.*, vol. 11, pp. 1178–1181, 2012.

[21] C. Bencivenni, M. V. Ivashina, R. Maaskant, and J. Wettergren, "Synthesis of maximally sparse arrays using compressive sensing and full-wave analysis for global earth coverage applications," *IEEE Trans. Antennas Propag.*, vol. 64, no. 11, pp. 4872–4877, Jul. 2016.

[22] Y. Aslan, A. Roederer, and A. Yarovoy, "Synthesis of quasi-modular circularly polarized 5G base station antenna arrays based on irregular clustering and sequential rotation," *Microw. Opt. Technol. Lett.*, to be published, doi: 10.1002/mop.32735.

[23] M. Lobo, L. Vandenberghe, S. Boyd, and H. Lebret, "Applications of second-order cone programming," *Linear Algebra Appl.*, vol. 284, no. 1–3, pp. 193–228, 1998.

[24] M. Grant and S. Boyd, "CVX: Matlab software for disciplined convex programming, version 2.1," Mar. 2014. [Online]. Available: http://cvxr.com/cvx, Mar. 2014.

[25] Y. Aslan, J. Puskely, A. Roederer, and A. Yarovoy, "Phase-only control of peak sidelobe level and pattern nulls using iterative phase perturbations," *IEEE Antennas Wireless Propag. Lett.*, vol. 18, no. 10, pp. 2081–2085, Aug. 2019.

[26] Y. Aslan, M. Candotti, and A. Yarovoy, "Synthesis of multi-beam space-tapered linear arrays with side lobe level minimization in the presence of mutual coupling," in *Proc. 13th EuCAP*, Krakow, Poland, Apr. 2019.
[27] H. B. Van, S. N. Jha, and C. Craeye, "Fast full-wave synthesis of printed antenna arrays including mutual coupling," *IEEE Trans. Antennas Propag.*, vol. 64, no. 12, pp. 5163–5171, Dec. 2016.
[28] V. Degli-Esposti *et al.*, "Ray-tracing-based mm-wave beamforming assessment," *IEEE Access*, vol. 2, pp. 1314–1325, 2014.
[29] Y. Aslan, J. Puskely, A. Roederer, and A. Yarovoy, "Performance comparison of single- and multi-lobe antenna arrays in 5G urban outdoor environments at mm-waves via intelligent ray tracing," in *Proc. 14th Eur. Conf. Antennas Propag.*, Copenhagen, Denmark, Mar. 2020, pp. 1–5.
[30] G. Oliveri, G. Gottardi, and A. Massa, "A new meta-paradigm for the synthesis of antenna arrays for future wireless communications," *IEEE Trans. Antennas Propag.*, vol. 67, no. 6, pp. 3774–3788, Jun. 2019.
[31] N. Anselmi, G. Gottardi, P. Rocca, G. Oliveri, and A. Massa, "Unconventional M-MIMO phased array design for 5G wireless systems," in *Proc. IEEE Int. Symp. Phased Array Syst. Technol.*, Waltham, MA, USA, Oct. 2019, pp. 1–3.
[32] H. Q. Ngo, *Massive MIMO: Fundamentals and System Designs*. Nottingham, U.K.: Linkoping Univ. Electron. Press, 2015.
[33] A. A. Glazunov, "Impact of deficient array antenna elements on downlink massive MIMO performance in RIMP and random-LoS channels," in *Proc. 12th Eur. Conf. Antennas Propag.*, London, U.K., Apr. 2018, pp. 1–4.
[34] C.-S. Park, Y.-S. Byun, A. M. Bokiye, and Y.-H. Lee, "Complexity reduced zero-forcing beamforming in massive MIMO systems," in *Proc. IEEE Inf. Theory Appl. Workshop*, San Diego, CA, USA, Feb. 2014, pp. 1–5.
[35] "A straight path towards 5G," White Paper, Straight Path Communications Inc., Sep. 2015.
[36] Z. Pi and F. Khan, "An introduction to millimeter-wave mobile broadband systems," *IEEE Commun. Mag.*, vol. 49, no. 6, pp. 101–107, Jun. 2011.
[37] "Two-resistor compact thermal model guideline," JESD-1, JEDEC, Jul. 2008.
[38] Y. Aslan, J. Puskely, A. Roederer, and A. Yarovoy, "Heat transfer enhancement in passively cooled 5G base station antennas using thick ground planes," in *Proc. 13th Eur. Conf. Antennas Propag.*, Krakow, Poland, Apr. 2019, pp. 1–5.
[39] C. A. Balanis, *Antenna Theory: Analysis and Design*. Hoboken, NJ, USA: Wiley, 2016.
[40] L. Bui, N. Anselmi, T. Isernia, P. Rocca, and A. Morabito, "On bandwidth maximization of fixed-geometry arrays through convex programming," *J. Electromagnet. Wave.*, vol. 34, no. 5, pp. 581–600, 2020.
[41] C. Bencivenni, A. A. Glazunov, R. Maaskant, and M. V. Ivashina, "Effects of regular and aperiodic array layout in multi-user MIMO applications," in *Proc. IEEE USNC/URSI NRSM*, San Diego, CA, USA, Jul. 2017, pp. 1877–1878.
[42] Y. Aslan, S. Salman, J. Puskely, A. Roederer, and A. Yarovoy, "5G multi-user system simulations in line-of-sight with space-tapered cellular base station phased arrays," in *Proc. 13th Eur. Conf. Antennas Propag.*, Krakow, Poland, Apr. 2019, pp. 1–5.
[43] D. Nicholls, *System Reliability Toolkit*. Utica, NY, USA: Reliability Information Analysis Center/Data and Analysis Center for Software, 2005.

Yanki Aslan (Graduate Student Member, IEEE) was born in Ankara, Turkey, in 1991. He received the B.Sc. degree with double specialization in communications and microwaves and antennas from Middle East Technical University, Ankara, Turkey, in 2014, the M.Sc. (*cum laude honor*) degree in electrical engineering, telecommunications, and sensing systems track from Delft University of Technology, Delft, the Netherland, in 2016.

In October 2016, he joined the Microwave Sensing, Signals, and Systems group as a Ph.D. candidate. He is working on the project "Antenna Topologies and Front-End Configurations for Multiple Beam Generation," which is a part of STW & NXP Partnership Program on "Advanced 5G Solutions." His research interests include multibeam antennas, array optimization methods, antenna front-end architectures, beamforming algorithms, communication system modeling, and antenna cooling.

Mr. Aslan received the Justus and Louise van Effen Scholarship from Delft University of Technology. For his achievements during his Ph.D. project, he received the IEEE APS Doctoral Research Grant in 2018 and the first EuMA Internship Award in 2019.

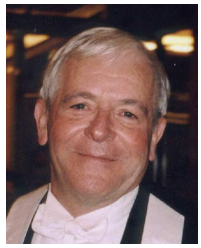

Antoine Roederer (Life Fellow, IEEE) was born in Paris in 1943. He received the B.S.E.E. degree from l'Ecole Superieure d'Electricite, Paris, France, in 1964, the M.S.E.E. degree from the University of California, Berkeley, CA, USA, with a Fulbright Fellowship, in 1965, and the Doctorate (Hons.) degree in electrical engineering from Universite de Paris VI, Paris, France, in 1972.

He was radar antenna R&D Engineer with THOMSON-CSF, Bagneux, France, during 1968–1973. He joined the European Space Research and Technology Centre of ESRO (now ESA, the European Space Agency), in Noordwjik, The Netherlands, in 1973. There, he initiated and supervised for many years R&D and project support for space antennas. In 1993, he became Head of the ESA's Electromagnetics Division. He has authored or coauthored more than 150 papers, several book chapters, and holds 20 patents in the field of antennas. This has included aspects of wideband communications, broadcasting, radar, and satellite antennas, with emphasis on log-periodics, reflectarrays, multiple beam reflectors, and arrays and advanced antenna feed networks. His current research interests include innovation and development in the field of radar and 5G base station antennas.

Dr Roederer was a recipient of numerous awards for his contributions to the field of antennas and to the antenna community in Europe. He has been Chairman of the EU COST 260 Project on Smart Antennas. He was the initiator and Chairman of the Millennium Conference on Antennas and Propagation, AP 2000 in Davos, precursor of the large EUCAP conferences. He retired from ESA in 2008. He is now a part-time Scientific Advisor at the Technical University of Delft, The Netherlands, from which he was awarded an honorary Doctorate.

Alexander Yarovoy (Fellow, IEEE) received the Diploma with honors in radio physics and electronics from the Kharkov State University, Kharkiv, Ukraine, in 1984 the Candidate Phys. & Math. Sci. and Doctor Phys. & Math. Sci. degrees in radiophysics in 1987 and 1994, respectively.

In 1987, he joined the Department of Radiophysics, Kharkov State University as a Researcher and became a Professor there in 1997. From 1994 to 1996, he was with the Technical University of Ilmenau, Germany as a Visiting Researcher. Since 1999, he has been with the Delft University of Technology, the Netherlands. Since 2009, he has been a Chair of Microwave Sensing, Systems, and Signals. He has authored and coauthored more than 450 scientific or technical papers, 4 patents and 14 book chapters, His main research interests are in high-resolution radar, microwave imaging and applied electromagnetics (in particular, UWB antennas).

Prof. Yarovoy served as a Guest-Editor of five special issues of the IEEE transactions and other journals. Since 2011, he has been an Associate Editor of the *International Journal of Microwave and Wireless Technologies*. He is the recipient of the European Microwave Week Radar Award for the paper that best advances the state-of-the-art in radar technology in 2001 (together with L.P. Ligthart and P. van Genderen) and in 2012 (together with T. Savelyev). In 2010 together with D. Caratelli, he got the Best Paper Award of the Applied Computational Electromagnetic Society (ACES). He served as the Chair and TPC Chair of the 5th European Radar Conference (EuRAD'08), Amsterdam, the Netherlands, as well as the Secretary of the 1st European Radar Conference (EuRAD'04), Amsterdam, the Netherlands. He also served as the Co-Chair and TPC Chair of the 10th International Conference on GPR (GPR2004) in Delft, the Netherlands. In 2008–2017, he served as Director of the European Microwave Association (EuMA).